J. Fluid Mech. (2025), *vol*. 1002, A12, doi:10.1017/jfm.2024.1176

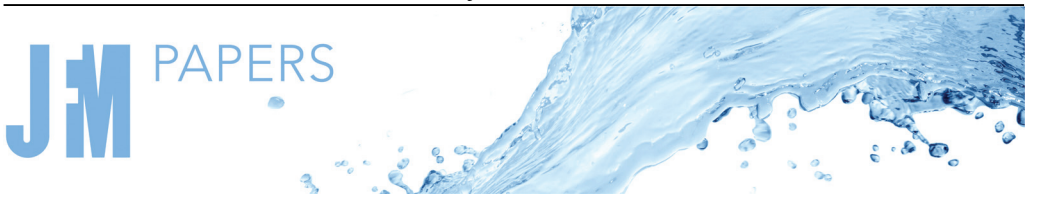

Scaling analysis for the frequency of Ostwaldian and Newtonian bead-on-fibre flows

Chase T. Gabbard[1], **James T. Rhoads**[2], **Jean-Marc Delhaye**[2] and **Joshua B. Bostwick**[2],†

[1]School of Engineering, Brown University, Providence, RI 02912, USA

[2]Department of Mechanical Engineering, Clemson University, Clemson, SC 29631, USA

(Received 11 July 2024; revised 5 December 2024; accepted 5 December 2024)

Liquid flowing down a fibre readily destabilises into a train of beads, commonly called a bead-on-fibre pattern. Bead formation results from capillary-driven instability and gives rise to patterns with constant velocity and time-invariant bead frequency f whenever the instability is absolute. In this study, we develop a scaling law for f that relates the Strouhal number St and capillary number Ca for Ostwaldian power-law liquids with Newtonian liquids recovered as a limiting case. We validate our proposed scaling law by comparing it with prior experimental data and new experimental data using xanthan gum solutions to produce a low capillary number $Ca \leq 10^{-2}$ regime. The experimental data encompasses both Ostwaldian and Newtonian flow, as well as symmetric and asymmetric patterns, and we find the data collapses along the predicted trend across seven orders of magnitude in Ca. Our proposed scaling law is a powerful tool for studying and applying bead-on-fibre flows where f is critical, such as heat and mass transfer systems.

Key words: capillary flows, thin films, pattern formation

1. Introduction

Liquid flowing down a fibre may destabilise into a train of beads, commonly called a bead-on-fibre pattern. Bead formation may result from inertia-driven Kaptiza-like instability (Kapitza 1948) or capillary-driven Plateau–Rayleigh-like instability (Plateau 1873; Rayleigh 1878), depending on the liquid properties, flow rate and fibre properties. When the dominant instability is capillary driven, the liquid beads have highly curved interfaces and time-invariant bead properties. In addition, viscosity slows the beads

† Email address for correspondence: jbostwi@clemson.edu

making them ideal for direct-contact heat and mass transfer applications where large retention times τ_r increase efficiency (Hattori, Ishikawa & Mori 1994; Chinju, Uchiyama & Mori 2000). In such applications, it is desirable to control the interfacial area A available for heat and mass transfer along the length L of the fibre. The interfacial area is $A \approx \tau_r f A_b$, where f is the bead frequency and A_b is the interfacial area of a bead. Thus, f is a key parameter for optimising bead-on-fibre flows for applications. Here, we derive a scaling law for f of an Ostwaldian fluid with power-law rheology, of which a Newtonian fluid is a limiting case, and validate it with new experiments coupled with experimental data from prior works, including symmetric and asymmetric bead profiles.

A thin liquid film coating on a horizontal fibre naturally destabilises into beads, similar to morning dew on a spider's web (Goren 1962), as shown in figure 1(*a*). On a vertically oriented fibre, this gravity-driven flow becomes unstable above a critical thickness (Quéré 1990; Kalliadasis & Chang 1994; Chang & Demekhin 1999). Early studies, motivated by fibre withdrawal from liquid baths (Lin & Liu 1975), examined the nonlinear evolution equations governing these wavy flows (Frenkel 1992; Trifonov 1992). For continuous flow down a fibre, Hattori *et al.* (1994) and Kliakhandler, Davis & Bankoff (2001) observed bead-on-fibre patterns characterised by three dynamic regimes, (i) convective (C), (ii) Plateau–Rayleigh (PR) and (iii) isolated (I), as shown in figure 1(*b*). Isolated patterns appear at low flow rates and have equally spaced beads moving at a constant velocity connected by an undulating film that also results from capillary instability. As flow rate increases, bead spacing decreases, leading to the Plateau–Rayleigh regime, where the film between beads lacks sufficient time to destabilise. At higher flow rates, inertia dominates, resulting in the convective regime characterised by interactive dynamics and irregular bead properties. Transitions between regimes provide insight into the instability type and dominant mechanism. For example, the shift from a single bead frequency (I and PR regime) to a broad frequency distribution (C regime) reflects the transition from an absolute instability to a convective instability (Duprat *et al.* 2007). However, bound state formation may result in multiple preferred wavelengths in the C regime when dispersive and dissipative effects are strong (Duprat *et al.* 2009*a*). Furthermore, drop-like beads in the I and PR regimes arise from capillary-driven instability at low flow rates, while wave-like beads emerge at higher flow rates due to inertial instability (Duprat, Ruyer-Quil & Giorgiutti-Dauphiné 2009*b*). These features were examined by Ruyer-Quil & Kalliadasis (2012) for the two-equation model derived by Ruyer-Quil *et al.* (2008) and single evolution equation derived by Craster & Matar (2006). Ruyer-Quil & Kalliadasis (2012) adopt scalings where the radial length scale is the flat-film thickness $L \mathrel{\widehat{=}} h$ determined by neglecting destabilising terms, the axial length scale is $L \mathrel{\widehat{=}} \kappa h$ where $\kappa \mathrel{\widehat{=}} (\sigma/\rho g h^2)^{1/3}$ reflects the balance between capillary pressure and hydrostatic pressure, and the time scale is defined based on h. These scalings hold in the long-wavelength limit but break down when the instability is absolute and the film evolves into highly curved drop-like beads at high bead frequency f. In this case, Ruyer-Quil & Kalliadasis (2012) noted an alternative scaling

$$\tau \mathrel{\widehat{=}} (\mu/\rho g r), \tag{1.1}$$

which compares gravity acceleration with momentum diffusion.

The bead morphology, describing the eccentricity of the beads relative to the fibre, can be either symmetric or asymmetric, as shown in figures 1(*c*) and 1(*d*). Hattori *et al.* (1994) first observed the transition from symmetric to asymmetric beads in high-surface-energy liquids. Gabbard & Bostwick (2021*a*) later showed that increasing surface tension σ and fibre radius r leads to asymmetric flow, characterised by faster-moving beads and larger

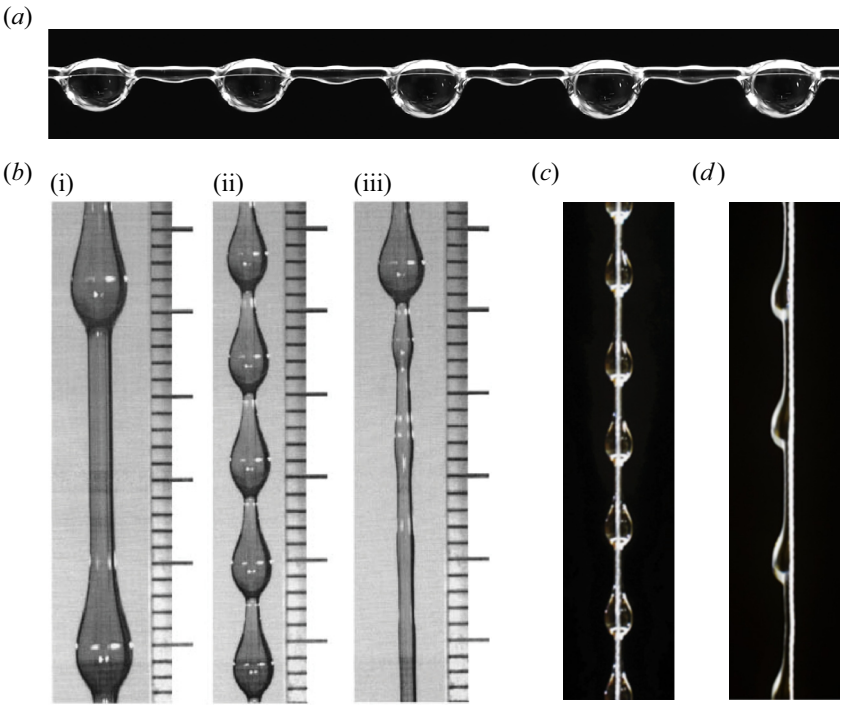

Figure 1. Bead-on-fibre patterns. (*a*) Beads on a horizontal fibre. (*b*) Three primary dynamical regimes observed in flow down a vertically-hung fibre as flow rate Q is decreased: (i) convective, (ii) Plateau–Rayleigh and (iii) isolated (reproduced from Kliakhandler *et al.* 2001). Beads can exhibit either (*c*) symmetric or (*d*) asymmetric morphology (reproduced from Gabbard & Bostwick 2021*a*).

bead spacing. Drops of low-surface-energy oils have also been observed flowing in a metastable asymmetric configuration (Gilet, Terwagne & Vandewalle 2010), and Eghbali *et al.* (2022) showed that quasi-inertialess flow down eccentric fibres can destabilise into a train of asymmetric beads. In addition, shear-thinning behaviour promotes asymmetry in polymer solutions (Gabbard & Bostwick 2023). In the case of shear-thinning liquids, the rheological behaviour is often modelled using the Ostwald power-law model

$$\mu = \beta \dot{\gamma}^{n-1}, \tag{1.2}$$

where μ is dynamic viscosity, β is the fluid consistency index, $\dot{\gamma}$ is shear rate and n is the power law index. For Newtonian fluids $n = 1$ and $\beta = \mu$, whereas $n < 1$ for shear-thinning fluids. This model has been used to explore shear-thinning and shear-thickening effects in drops flowing down vertical fibres (Yu & Hinch 2014). Boulogne, Pauchard & Giorgiutti-Dauphiné (2012) explored the flow of polymer solutions on a fibre, finding that decreasing n leads to thinner pre-instability films and a transition in the velocity profile from parabolic to plug-like. While these effects modify the growth rate of capillary instability, they maintain the same underlying time scale for drop-like beads, as discussed by Ruyer-Quil & Kalliadasis (2012), with adjustments for shear-thinning: $\tau \mathrel{\widehat{=}} (\beta/\rho g r)^{1/n}$. These studies illustrate the wide range of bead-on-fibre patterns. Despite this, a comprehensive understanding of the bead dynamics is lacking.

Specifically, a unifying scaling for the frequency of beads is critical for designing and optimising heat and mass transfer applications such as CO_2 separation (Chinju *et al.* 2000; Uchiyama *et al.* 2003; Migita, Soga & Mori 2005; Wagstaff *et al.* 2024), gas-side

mass transfer (Grünig *et al.* 2012), direct-contact heat exchange (Hattori *et al.* 1994; Zeng *et al.* 2017; Zeng, Sadeghpour & Ju 2018), desalination (Sadeghpour *et al.* 2019; Zeng, Sadeghpour & Ju 2019), fine and ultrafine particle collection (Sadeghpour *et al.* 2021) and liquid–liquid extraction (Zhang, Liu & Chen 2023; Chang *et al.* 2024). Bead-on-fibre flow has also been proposed as an ideal low-energy alternative for vacuum distillation applications (Grünig, Skale & Kraume 2010) and observed in fibre-based fog harvesting applications (Shi *et al.* 2018; Labbé & Duprat 2019; Moncuquet *et al.* 2022). Bead-on-fibre flow gained popularity as an effective alternative to traditional direct-contact systems after being introduced by Hattori *et al.* (1994) for heat exchange, and later for mass transfer (Chinju *et al.* 2000). These early studies showed that viscous shear increased the bead retention time compared with free-falling drops in commercial spray towers and exhibited enhanced mixing due to a velocity mismatch between the beads and their connecting films. These systems also help regularise the bead density and show that film waviness enhances mass transfer compared to planar films (Grünig *et al.* 2012), a feature which has been attributed to the ability of the high-curvature beads to serve as sinks for mass transfer (Sadeghpour *et al.* 2019). In addition, the smooth liquid–gas interface results in up to two orders of magnitude lower pressure drop across the system compared with a conventional packed-bed column (Migita *et al.* 2005) and an order of magnitude lower than comparable corrugated sheet structured packings (Grünig *et al.* 2010). The bead frequency f characterises the flow pattern and has an application-specific effect on system efficiency. For instance, Sadeghpour *et al.* (2019) found that mass transfer conductance in a humidification–dehumidification desalination system increases with decreasing bead spacing up to the transition between absolute and convective flow. Thus, a high f in the absolute regime is desirable for efficiency. Alternatively, Zeng *et al.* (2018) found that closely spaced beads associated with high f reduced the heat transfer coefficient. Thus, optimising system performance requires a detailed understanding of bead-on-fibre flow physics in order to tailor bead frequency for specific system requirements.

In this work, we address the timely need for predicting bead frequency across liquid rheology and bead morphology by deriving a scaling law for the bead frequency f, as it depends on the flow rate Q through dimensional analysis in § 2. Next, we describe our experimental protocol and image processing technique for extracting experimental data in § 3. In § 4, we test our scaling law a against an extensive experimental data set. We provide a brief discussion of our results with relevance to practical applications in § 5. We end by offering some concluding remarks in § 6.

2. Scaling analysis

Consider a fluid with surface tension σ, viscosity μ and density ρ flowing down a thin vertical fibre of radius r. The liquid film is uniform if the volume flow rate Q is low (Quéré 1990). If the flow rate increases, liquid beads appear on the film, as illustrated in figure 2(*a*). Our objective is to determine the steady-state frequency of the beads in terms of Q for an Ostwaldian fluid. In our analysis, we assume beads are drop-like and result from an absolutely unstable base flow such that the steady-state bead frequency f is single-valued and time-invariant. For such flows, we assume the primary factors influencing the frequency are the liquid properties, fibre size and flow rate.

2.1. *The scaling for Ostwaldian fluids*

The Ostwald–de Waele model (1.2) is a surrogate for the constitutive law of shear-thinning (i.e. pseudoplastic) or dilatant fluids. It expresses the shear stress τ_{ss} as a power law of the

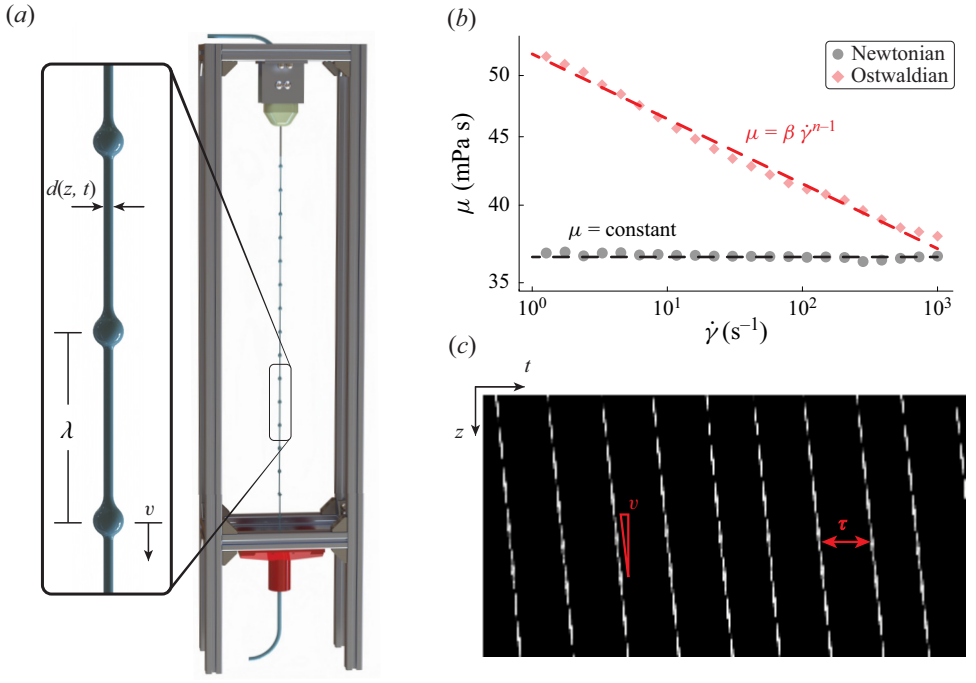

Figure 2. Experiment. (*a*) Schematic of the experimental apparatus with the inset showing the experimental variables. (*b*) Viscosity μ against shear rate $\dot{\gamma}$ for a Newtonian (gray circles) and Ostwaldian (red diamonds) liquid with dashed lines showing their best fit to a constant viscosity ($\mu = 36.6 \times 10^{-3}$ Pa s) and power-law model ($\beta = 51.9 \times 10^{-3}$ Pa s^n, $n = 0.95$), respectively. (*c*) Spatiotemporal diagram showing the global evolution of beads (white) for a bead-on-fibre pattern with constant bead velocity v and bead frequency $f = 1/\tau$.

shear rate $\dot{\gamma}$, i.e. the velocity gradient perpendicular to the plane of shear: $\tau_{ss} = \beta\dot{\gamma}^n$. The power-law index n is less than 1 for a shear-thinning (pseudoplastic) fluid and greater than 1 for a dilatant one. When $n = 1$, the liquid is Newtonian and the shear stress τ_{ss} is a linear function of shear rate $\dot{\gamma}$. As in SI units, the shear stress τ_{ss} is in Pa, the shear rate $\dot{\gamma}$ in s^{-1} and the fluid consistency index β is in Pa s^n. We must emphasise that the values of β and n are experimentally determined for a certain domain of validity, as shown in figure 2(*b*).

The motion of the film is impelled by gravity and impeded by the Ostwaldian consistency index β, which yields a characteristic time $\tau \mathrel{\widehat{=}} (\beta/\rho g r)^{1/n}$, also used by Boulogne *et al.* (2012) for polymer solutions. This definition entails the two quantities β and n that characterise an Ostwaldian fluid. Defining a gravity time $\tau_g \mathrel{\widehat{=}} (r/g)^{1/2}$ and a momentum diffusion time $\tau_d \mathrel{\widehat{=}} (\rho r^2/\beta)^{1/(2-n)}$ we obtain a physical significance of the Ostwaldian characteristic time $\tau \equiv (\tau_g^2/\tau_d^{2-n})^{1/n}$.

We now apply a physically-based dimensional analysis. First, we posit that the bead frequency f depends on the following quantities of interest: the characteristic time τ of the Ostwaldian fluid, the fibre radius r, the weight per unit volume ρg of the fluid, the surface tension σ and the volume flow rate Q of the fluid. Second, we note that two length dimensions exist: one L_r in the radial direction and the other L_z in the vertical direction. Adding base dimensions is a method introduced by Huntley (1952) and is known as vectorial or directional dimensional analysis. Expressing the dimensions of all the quantities of interest in terms of the minimum number of base dimensions required,

we get

$$\left.\begin{gathered}\dim[f] = T^{-1}, \quad \dim[\tau] = T, \quad \dim[Q] = L_r^2 L_z T^{-1}, \\ \dim[r] = L_r, \quad \dim[\rho g] = M L_r^{-2} T^{-2}, \quad \dim[\sigma] = M L_r^{-1} L_z T^{-2}.\end{gathered}\right\} \tag{2.1}$$

As we have six quantities of interest and four base dimensions, the Pi-theorem yields two dimensionless groups for describing the problem. Making all the quantities of interest dimensionless, we obtain

$$\left.\begin{array}{cccccc} \dfrac{f}{T^{-1}} & \dfrac{\tau}{T} & \dfrac{Q}{L_r^2 L_z T^{-1}} & \dfrac{r}{L_r} & \dfrac{\rho g}{M L_r^{-2} T^{-2}} & \dfrac{\sigma}{M L_r^{-1} L_z T^{-2}}. \\ (1) & (2) & (3) & (4) & (5) & (6) \end{array}\right\} \tag{2.2}$$

Choosing a yardstick for each base dimension, starting with the simplest:

$$\left.\begin{gathered}(2) \Rightarrow T = \tau \quad (4) \Rightarrow L_r = r, \\ (3) \Rightarrow L_z = \frac{Q\tau}{r^2} \quad (6) \Rightarrow M = \frac{\sigma r^3 \tau}{Q},\end{gathered}\right\} \tag{2.3}$$

the two Pi-terms immediately appear,

$$(1) \Rightarrow \Pi_1 \mathrel{\widehat{=}} f\tau \quad (5) \Rightarrow \Pi_2 \mathrel{\widehat{=}} \frac{\rho g Q \tau}{\sigma r}. \tag{2.4}$$

Let us now look for the physical interpretations of the two Pi-terms. By analogy with a Newtonian fluid for which $\beta \equiv \mu$ and $n = 1$, the dimensionless frequency Π_1 is the ratio of the bead frequency f to the scale gr/ν of the kinematic wave frequency that may propagate on the surface of the liquid film, where $\nu = \mu/\rho$ is the kinematic viscosity. As the speed of a kinematic wave is three times the average velocity of the film, Π_1 can be considered the product of the measured frequency by the film advective time scale. Consequently, Π_1 can be thought of as a Strouhal number $St \mathrel{\widehat{=}} f\tau$.

By using the same analogy, and to parallel the Newtonian case ($\beta \equiv \mu, n = 1$), the dimensionless volume flow rate Π_2 can be interpreted as a capillary number $Ca \mathrel{\widehat{=}} (\rho g Q \tau)/(\sigma r)$.

2.2. *The Newtonian limit $n \to 1$*

In the limit $n \to 1$, $\beta \equiv \mu$ and Newtonian flow is recovered. Here, the viscogravitational time scale $\tau \equiv (\tau_g^2/\tau_d^{2-n})^{1/n}$ reduces to (1.1). The Pi-terms in (2.4) simplify to

$$(1) \Rightarrow \Pi_1 \mathrel{\widehat{=}} \frac{f\mu}{\rho g r}, \quad (5) \Rightarrow \Pi_2 \mathrel{\widehat{=}} \frac{\mu Q}{\sigma r^2}, \tag{2.5}$$

where Π_1 is the Strouhal number $St \mathrel{\widehat{=}} (f\mu)/(\rho g r)$ and Π_2 is the capillary number $Ca \mathrel{\widehat{=}} (\mu Q)/(\sigma r^2)$.

3. Experiment

We performed experiments using an apparatus composed of an aluminium frame, a 3D-printed liquid reservoir, and a custom nozzle housing that ensured the liquid was applied concentric to the fibre, as shown in figure 2(*a*). The apparatus was mounted on

a pneumatic optical table to minimise external vibrations and preserve spatial calibrations. The fibres used were nylon monofilament with radius ranging from $0.9\,\text{mm} \leq r \leq 1.5\,\text{mm}$, and the nozzle was stainless steel with radius $r_n = 1.15$ mm. Before each experiment, a clean fibre was pinned at the top and bottom of the apparatus and manually tensioned. A precision syringe pump (NE-1000) applied the working fluid to the fibre at a flow rate Q and the resulting bead-on-fibre patterns were characterised by the bead velocity v and wavelength λ, shown in the inset of figure 2(*a*).

The working fluids were solutions of xanthan gum (XG), a rod-like polymer with shear-thinning behaviour and negligible elasticity, dissolved in mixtures of distilled water and glycerol. Solutions were prepared by mixing the water and glycerol until the solution appeared homogenous, adding a prescribed concentration $0\,\text{ppm} \leq \Phi \leq 3000\,\text{ppm}$ of XG to the solution, and stirring the solution with a magnetic stirrer for at least 24 hours. All solutions were tested shortly after synthesis to avoid phase separation. The surface tension $\sigma = 0.051 - 0.065\,\text{N}\,\text{m}^{-1}$ and density $\rho = 1204\text{–}1224\,\text{kg}\,\text{m}^{-3}$ of each solution were measured with an Attension Sigma 702 tensiometer with a Whilhelmy plate and density probe, respectively. In our experiments the capillary length $\ell_c \mathrel{\widehat{=}} (\sigma/\rho g)^{1/2}$ ranged from 2.1 to 2.3 mm. Up to now, most bead frequency data were collected using thin fibres with radius $r \leq 0.5$ mm despite bead-on-fibre flows emerging on fibres up to $r \approx 0.8$ mm, above which the film remains uniform (Hattori *et al.* 1994). Here, we fill in this missing data by testing thick fibres $0.5\,\text{mm} \leq r \leq 0.75\,\text{mm}$ such that the axial and azimuthal interfacial curvature are comparable, as described by the Goucher number $Go \mathrel{\widehat{=}} r/\ell_c = 0.22\text{–}0.36$. The viscosity μ was measured against shear rate $\dot{\gamma}$ using a standard shear rate sweep from 0.1 to $1000\,\text{s}^{-1}$ performed on an Anton-Paar 302 shear rheometer with a cone and plate configuration, as shown in figure 2(*b*) for a 0 ppm (Newtonian) and 50 ppm (Ostwaldian) XG solution. The rheology was characterised by an Ostwald power-law model with a consistency index β from 37×10^{-3} to $1538 \times 10^{-3}\,\text{Pa}\,\text{s}^n$ and power law index n from 0.53 to 1 for all solutions tested. For the limiting case of a Newtonian fluid, $n = 1$ and $\beta = \mu$.

We began each set of experiments by flushing the system with IPA and inserting a new fibre. The liquid was then applied to the fibre, readily destabilising into a bead-on-fibre pattern that could be symmetric or asymmetric, depending on the solution and fibre radius. A Chronos 2.1-HD high-speed camera (Kron Technologies) or a Nikon D3500 DSLR camera was used to record the pattern, which was illuminated from the side by a Godox SL200III studio light and an LED panel. Videos were recorded approximately 500 mm beneath the nozzle and the liquid was continuously applied for up to 20 minutes before recording to ensure steady-state dynamics. The videos were analysed by tracking a column of pixels intersecting the widest part of the flowing beads giving rise to the spatiotemporal diagram shown in figure 2(*c*). The slope of the white lines measures the bead velocity v, which is constant and consistent across all beads when the lines are straight and parallel. The horizontal spacing between lines measures the time τ between two beads passing the same point giving a frequency $f = 1/\tau$. Herein, we restrict our study to patterns with constant frequency and regular dynamics. The random error for each experiment was calculated by recording a large number of beads and using the built-in standard deviation MATLAB function.

4. Results

To test the scaling law derived in § 2, we combined frequency data from seven prior studies (Duprat *et al.* 2007; Sadeghpour, Zeng & Ju 2017; Sadeghpour *et al.* 2019;

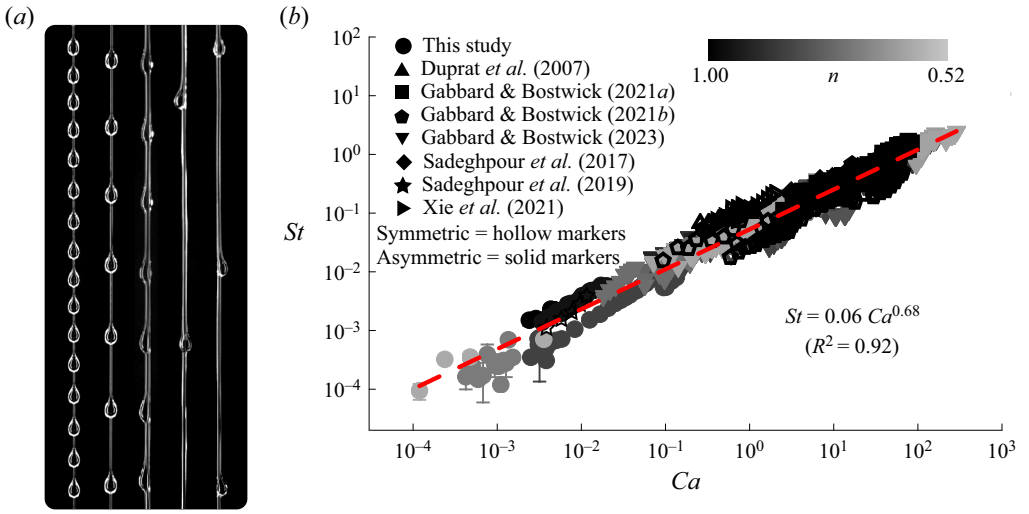

Figure 3. (*a*) Bead-on-fibre patterns for $Ca \approx 10^{-1}$. (*b*) Strouhal number $St \mathrel{\widehat{=}} f\tau = f(\beta/\rho g r)^{1/n}$ plotted against capillary number $Ca \mathrel{\widehat{=}} (\rho g Q \tau)/(\sigma r)$ for symmetric (hollow markers) and asymmetric (solid markers) bead-on-fibre patterns. Marker shape indicates the data source and marker shading corresponds to the shear-thinning index n following the shading scale bar. The dashed red lines shows a best-fit power-law trend $St = 0.06\, Ca^{0.68}$ with goodness-of-fit $R^2 = 0.92$.

Gabbard & Bostwick 2021*a*,*b*, 2023; Xie *et al.* 2021) with our new experimental results. This extensive data set contains 1061 experiments, including symmetric and asymmetric patterns, Ostwaldian and Newtonian working liquids, fibre radii ranging from 0.1 to 1.5 mm and flow rates ranging from 0.01 to 180.56 $\mathrm{mm^3\,s^{-1}}$. Table 1 provides the morphology, power-law index n, Goucher number Go and capillary number Ca for each data source. Our new data for large fibres and shear-thinning solutions extend the range of Ca by two decades, giving a total range $10^{-4} \leq Ca \leq 10^{3}$.

A variety of patterns are observed across the data, such that even data with similar Ca may exhibit stark differences in bead profiles and spacing λ, as demonstrated in figure 3(*a*) for patterns with $Ca \approx 10^{-1}$ and n decreasing from 1 to 0.53 (left to right). In this example, shear thinning promotes asymmetry, leading to a comparable increase in speed and spacing of beads. Figure 3(*b*) plots the Strouhal number St against capillary number Ca for the symmetric (hollow markers) and asymmetric (solid markers) bead-on-fibre data represented in table 1. The plot marker shape denotes the source and the marker shading indicates the value of the power-law index n. The data collapses along a single power-law trend, shown as a red dashed line. Here the best-fit trend is $St = 0.06\, Ca^{0.68}$ with goodness-of-fit $R^2 = 0.92$. Thus, we find strong evidence for the proposed scaling law across an extensive range of Ca.

Interestingly, Ruyer-Quil & Kalliadasis (2012) observed that the velocity of drop-like beads is strongly influenced by the thickness of the residual film, which is controlled by the capillary number $Ca = \mu v/\sigma$. They found that the film thickness exhibits a dependency on $Ca^{2/3}$, drawing a direct analogy to the classic Landau–Levich–Derjaguin law. In this process, the bead velocity governs the film thickness, which then affects the motion of subsequent beads, establishing a dynamic equilibrium. We propose that this same mechanism, where the flow dynamics depend on the film thickness, underlies the $Ca^{2/3}$ dependency we observe.

Source	Morphology	n	Go	Ca
This study	Symmetric, asymmetric	0.53–1	0.22–0.36	10^{-4}–10^{-2}
Duprat *et al.* (2007)	Symmetric	1	0.22	10^{-1}–10^{0}
Gabbard & Bostwick (2021*a*)	Symmetric, asymmetric	1	0.04–0.14	10^{-2}–10^{2}
Gabbard & Bostwick (2021*b*)	Symmetric	1	0.03–0.16	10^{-2}–10^{3}
Gabbard & Bostwick (2023)	Symmetric, asymmetric	0.52–1	0.02–0.19	10^{-2}–10^{3}
Sadeghpour *et al.* (2017)	Symmetric	1	0.07–0.15	10^{0}–10^{1}
Sadeghpour *et al.* (2019)	Symmetric	1	0.14	10^{-3}–10^{-2}
Xie *et al.* (2021)	Symmetric	1	0.17	10^{-1}–10^{0}

Table 1. Data source with reported flow morphology, shear-thinning index n, Goucher number Go and capillary number Ca.

5. Discussion

We have validated a scaling law for St across seven decades of Ca. Our extensive data set includes changes in experimental variables that are assumed negligible in the dimensional analysis. These features include the nozzle radius r_n, which ranged from 0.5 to 3.2 mm in Sadeghpour *et al.* (2017) and 0.4 to 3.3 mm in Gabbard & Bostwick (2021*b*), whose role in altering the dynamical regime was first noted by Chinju *et al.* (2000) and later modelled by Ji *et al.* (2020). The orientation of the nozzle relative to the fibre is also varied within our data set, where three studies orient the nozzle perpendicular to the fibre while the others, including the current experiments, use a concentric nozzle–fibre orientation. Notably, the same qualitative regimes emerge for both orientations but with slight quantitative differences, specifically in the transition flow rate between regimes (Gabbard & Bostwick 2021*a*). Despite this, our proposed scaling law accurately captures the frequency behaviour over several orders of Ca and is insensitive to boundary conditions at the nozzle. Different fibre types were used in the studies we examined, including nylon monofilament, nylon multifilament and cotton threads. Similar to nozzle orientation, fibre properties play a minor role in augmenting general variable dependencies but can affect patterns quantitatively. In these cases, a slip coefficient λ has been introduced to improve model predictions (Sadeghpour *et al.* 2019). We demonstrate that our proposed scaling law is robust to fibre properties by including the results of Xie *et al.* (2021), who used fibres with different cross-sectional shapes. We expect our results to become invalid for more exotic fibre shapes or multiple fibre arrangements, which are capable of suppressing capillary instability (Wang *et al.* 2020; Gabbard, Rhoads & Bostwick 2024; Xu *et al.* 2024).

The empirical agreement between our dataset and the scaling law derived in § 2 highlights the dominant factors governing bead frequency. Despite this, several assumptions and unexplored physics limit its applicability outside this range. The scaling is derived for unstable flow down a fibre in the absolute regime, requiring a capillary number Ca large enough to avoid nonlinear saturation inhibiting bead growth (Quéré 1990) but low enough to remain below the absolute/convective threshold (Duprat *et al.* 2007). Beyond this threshold, bead-like drops become wave-like, necessitating a different axial length scale (Ruyer-Quil & Kalliadasis 2012), and statistical approaches may better capture frequency behaviour. Newtonian and shear-thinning fluids modelled by (1.2) align with the derived scaling. This rheological model is valid for the moderate shear rates typical for flow down a fibre but may be less accurate in the high- and low-shear rate limits. We have not currently explored these limits in the studies discussed herein. Using thicker,

thinner fibres and a more complex rheological description of the liquid behaviour could quantitatively specify these limits. In addition, while some experiments in our dataset used surfactant to promote flow symmetry (Boulogne *et al.* 2012; Gabbard & Bostwick 2021*a*, 2023), surfactant kinetics were not fully explored. Prior studies on fibre coatings show a complex relationship between surfactant concentration and coating thickness (Shen *et al.* 2002), with high surfactant concentrations shown to suppress instability (Boulogne *et al.* 2013). Similar thickening effects have been observed in polymer solutions due to normal stresses (De Ryck & Quéré 1998). The role of elasticity on bead frequency is not fully understood and may limit the applicability of our results, necessitating further experimental investigation. In summary, while the proposed scaling law captures key physics for most practical liquids, its applicability is limited and highly elastic fluids or those with high surfactant concentrations may present dynamics that deviate from our prediction.

5.1. *Optimising bead-on-fibre flows*

As discussed in § 1, bead-on-fibre flows have emerged as a promising solution for direct-contact heat exchangers and mass transfer applications. The effect of bead frequency on performance, whether enhancing (Sadeghpour *et al.* 2019) or degrading (Zeng *et al.* 2018), depends on the specific application. In either case, our scaling law provides a design tool for optimising bead-on-fibre patterns, complementing theoretical thresholds for absolute instability (Duprat *et al.* 2007) and empirical guidelines for flow morphology (Gabbard & Bostwick 2021*a*, 2023) to form a comprehensive framework for efficient design. For example, consider the application of bead-on-fibre flow as a direct-contact condenser in a humidification–dehumidification desalination system (Sadeghpour *et al.* 2019). In this case, high bead curvature and long retention times are desired, favouring a symmetric flow morphology, which offers higher bead density and retention. Guidelines for producing symmetric flows can be applied first. As bead frequency increases with flow rate Q, mass transfer conductance improves, up to the transition from absolutely to convectively unstable flow. Beyond this transition, further increases in water demand reduce system efficiency, as higher flow rates no longer boost mass transfer. Thus, the absolute/convective transition threshold (Duprat *et al.* 2007) serves as the next design constraint. Once the symmetric absolutely unstable flow regime is defined, our scaling law can approximate the maximum bead frequency within this parameter space. This design approach is broadly applicable but may require further refinement for specific cases, such as enhancing fibre composites with curable liquids (Ghosh, Greenfeld & Wagner 2023), liquid-liquid extraction systems, such as those proposed for lithium recovery from salt lake brines (Chang *et al.* 2024), or counterflow systems with high counterflow velocities, which reduce bead frequency significantly and alter bead shape (Grünig *et al.* 2010).

6. Concluding remarks

We have derived a robust and comprehensive scaling law for the steady-state bead frequency f of an absolutely unstable thin film flowing down a fibre, which relates a generalised Strouhal number St to the capillary number Ca for an Ostwaldian fluid with a Newtonian fluid as a limiting case. We verified our scaling analysis using experimental data from seven prior works (Duprat *et al.* 2007; Sadeghpour *et al.* 2017, 2019; Gabbard & Bostwick 2021*a*,*b*, 2023; Xie *et al.* 2021) and new experiments performed with XG polymer solutions on large fibres, specifically selected to expand the range of Ca. The data spans seven orders of magnitude in Ca and fits a power-law trend of the form

Solution	Φ (ppm)	ρ (kg m^{-3})	σ (N m^{-1})	n (−)	β (Pa s^n)
1	0	1205	59	1	37
2	50	1204	52	0.96	49
3	250	1206	51	0.82	130
4	1000	1219	63	0.66	491
5	3000	1224	65	0.53	1538

Table 2. Composition and properties of solutions used for low-Ca data.

$St \sim Ca^{2/3}$. Furthermore, the data include a diverse set of bead-on-fibre patterns including axially symmetric and asymmetric patterns, which have previously been shown to exhibit significantly different dynamics (Gabbard & Bostwick 2021*a*, 2023). Thus, our results provide valuable insight into the underlying physics that govern bead-on-fibre flows, irrespective of fibre radius r, flow rate Q, bead morphology, nozzle radius r_n and nozzle orientation.

The agreement between empirical data and our proposed scaling law supports the use of the viscogravitational time scale first introduced by Ruyer-Quil & Kalliadasis (2012) for drop-like beads and later adapted for shear-thinning flow by Boulogne *et al.* (2012). Recent research has further explored flow down fibres, revealing insights that mimic natural processes and enable advanced control in practical applications. These studies provide numerous opportunities to expand and test our findings for bead-on-fibre flow, including the use of other complex fluids such as shear-thickening and viscoelastic solutions, and systems involving soft (Chao *et al.* 2024), grooved (Leonard *et al.* 2023), twisted (Kern & Carlson 2024; Van Hulle *et al.* 2024) or spaced fibres (Gabbard & Bostwick 2024; Gabbard *et al.* 2024). Moreover, our work draws inspiration from real-world applications, offering a valuable basis for future comparisons in more complex settings, such as in cross-flow (Cazaubiel & Carlson 2023), counterflow (Grünig *et al.* 2010) or configurations involving closely spaced fibres (Wagstaff *et al.* 2023). Evaluating the performance of our scaling in these diverse settings will be critical for optimising bead-on-fibre systems for industrial applications.

Funding. J.B.B. acknowledges support from the NSF (grant number CMMI-1935590). This project is partially supported by the Clemson University Creative Inquiry program.

Declaration of interests. The authors report no conflict of interest.

Author ORCIDs.
Chase T. Gabbard https://orcid.org/0009-0006-4412-4066;
Joshua B. Bostwick https://orcid.org/0000-0001-7573-2108.

Appendix. Solution properties

The liquid properties used for the low-Ca experiments reported here are listed in table 2.

References

Boulogne, F., Fardin, M.-A., Lerouge, S., Pauchard, L. & Giorgiutti-Dauphiné, F. 2013 Suppression of the Rayleigh–Plateau instability on a vertical fibre coated with wormlike micelle solutions. *Soft Matt.* **9** (32), 7787–7796.

Boulogne, F., Pauchard, L. & Giorgiutti-Dauphiné, F. 2012 Instability and morphology of polymer solutions coating a fibre. *J. Fluid Mech.* **704**, 232–250.

CAZAUBIEL, A. & CARLSON, A. 2023 Influence of wind on a viscous liquid film flowing down a thread. *Phys. Rev. Fluids* **8** (5), 054002.

CHANG, C., ZHENG, Q., XU, D., WANG, Y., SU, H. & KUANG, S. 2024 A scalable extraction column utilizing discrete liquid films for lithium recovery from salt lake brines. *J. Environ. Chem. Engng* **12** (5), 113706.

CHANG, H.-C. & DEMEKHIN, E.A. 1999 Mechanism for drop formation on a coated vertical fibre. *J. Fluid Mech.* **380**, 233–255.

CHAO, Y., ZHU, L., DING, Z., KONG, T., CHANG, J. & WANG, Z. 2024 Stability of gravity-driven viscous films flowing down a soft cylinder. *Phys. Rev. Fluids* **9** (9), 094001.

CHINJU, H., UCHIYAMA, K. & MORI, Y.H. 2000 'String-of-beads' flow of liquids on vertical wires for gas absorption. *AIChE J.* **46** (5), 937–945.

CRASTER, R.V. & MATAR, O.K. 2006 On viscous beads flowing down a vertical fibre. *J. Fluid Mech.* **553**, 85–105.

DE RYCK, A. & QUÉRÉ, D. 1998 Fluid coating from a polymer solution. *Langmuir* **14** (7), 1911–1914.

DUPRAT, C., GIORGIUTTI-DAUPHINÉ, F., TSELUIKO, D., SAPRYKIN, S. & KALLIADASIS, S. 2009*a* Liquid film coating a fiber as a model system for the formation of bound states in active dispersive-dissipative nonlinear media. *Phys. Rev. Lett.* **103** (23), 234501.

DUPRAT, C., RUYER-QUIL, C. & GIORGIUTTI-DAUPHINÉ, F. 2009*b* Spatial evolution of a film flowing down a fiber. *Phys. Fluids* **21** (4), 042109.

DUPRAT, C., RUYER-QUIL, C., KALLIADASIS, S. & GIORGIUTTI-DAUPHINÉ, F. 2007 Absolute and convective instabilities of a viscous film flowing down a vertical fiber. *Phys. Rev. Lett.* **98** (24), 244502.

EGHBALI, S., KEISER, L., BOUJO, E. & GALLAIRE, F. 2022 Whirling instability of an eccentric coated fibre. *J. Fluid Mech.* **952**, A33.

FRENKEL, A. 1992 Nonlinear theory of strongly undulating thin films flowing down vertical cylinders. *Europhys. Lett.* **18** (7), 583.

GABBARD, C.T. & BOSTWICK, J.B. 2021*a* Asymmetric instability in thin-film flow down a fiber. *Phys. Rev. Fluids* **6** (3), 034005.

GABBARD, C.T. & BOSTWICK, J.B. 2021*b* Scaling analysis of the Plateau–Rayleigh instability in thin film flow down a fiber. *Exp. Fluids* **62** (7), 141.

GABBARD, C.T. & BOSTWICK, J.B. 2023 Bead-on-fibre morphology in shear-thinning flow. *J. Fluid Mech.* **961**, A14.

GABBARD, C.T. & BOSTWICK, J.B. 2024 Gravity-driven flow of liquid bridges between vertical fibres. *J. Fluid Mech.* **997**, A74.

GABBARD, C.T., RHOADS, J.T. & BOSTWICK, J.B. 2024 Suppressing capillary instability in falling liquid threads. *J. Fluid Mech.* **1000**, A77.

GHOSH, S., GREENFELD, I. & WAGNER, H.D.ANIEL 2023 CNT coating and anchoring beads enhance interfacial adhesion in fiber composites. *Compos.* A **167**, 107427.

GILET, T., TERWAGNE, D. & VANDEWALLE, N. 2010 Droplets sliding on fibres. *Eur. Phys. J.* E **31**, 253–262.

GOREN, S.L. 1962 The instability of an annular thread of fluid. *J. Fluid Mech.* **12** (2), 309–319.

GRÜNIG, J., LYAGIN, E., HORN, S., SKALE, T. & KRAUME, M. 2012 Mass transfer characteristics of liquid films flowing down a vertical wire in a counter current gas flow. *Chem. Engng Sci.* **69** (1), 329–339.

GRÜNIG, J., SKALE, T. & KRAUME, M. 2010 Liquid flow on a vertical wire in a countercurrent gas flow. *Chem. Engng J.* **164** (1), 121–131.

HATTORI, K., ISHIKAWA, M. & MORI, Y.H. 1994 Strings of liquid beads for gas-liquid contact operations. *AIChE J.* **40** (12), 1983–1992.

HUNTLEY, H.E. 1952 *Dimensional Analysis*. Dover.

JI, H., SADEGHPOUR, A., JU, Y.S. & BERTOZZI, A.L. 2020 Modelling film flows down a fibre influenced by nozzle geometry. *J. Fluid Mech.* **901**, R6.

KALLIADASIS, S. & CHANG, H-C. 1994 Drop formation during coating of vertical fibres. *J. Fluid Mech.* **261**, 135–168.

KAPITZA, P.L. 1948 Wave flow of thin viscous fluid layers. *Zh. Eksp. Teor. Fiz.* **18**, 3–28.

KERN, V.R. & CARLSON, A. 2024 Twisted fibers enable drop flow control and enhance fog capture. *Proc. Natl Acad. Sci. USA* **121** (32), e2402252121.

KLIAKHANDLER, I.L., DAVIS, S.H. & BANKOFF, S.G. 2001 Viscous beads on vertical fibre. *J. Fluid Mech.* **429**, 381–390.

LABBÉ, R. & DUPRAT, C. 2019 Capturing aerosol droplets with fibers. *Soft Matt.* **15** (35), 6946–6951.

LEONARD, M., VAN HULLE, J., WEYER, F., TERWAGNE, D. & VANDEWALLE, N. 2023 Droplets sliding on single and multiple vertical fibers. *Phys. Rev. Fluids* **8** (10), 103601.

LIN, S.P. & LIU, W.C. 1975 Instability of film coating of wires and tubes. *AIChE J.* **21** (4), 775–782.

MIGITA, H., SOGA, K. & MORI, Y.H. 2005 Gas absorption in a wetted-wire column. *AIChE J.* **51** (8), 2190–2198.

MONCUQUET, A., MITRANESCU, A., MARCHAND, O.C., RAMANANARIVO, S. & DUPRAT, C. 2022 Collecting fog with vertical fibres: combined laboratory and in-situ study. *Atmos. Res.* **277**, 106312.

PLATEAU, J. 1873 *Statique expérimentale et théorique des liquides soumis aux seules forces moléculaires*. Tome Second, Gauthier-Villars.

QUÉRÉ, D. 1990 Thin films flowing on vertical fibers. *Europhys. Lett.* **13** (8), 721.

RAYLEIGH, LORD 1878 On the instability of jets. *Proc. Lond. Math. Soc.* **1** (1), 4–13.

RUYER-QUIL, C. & KALLIADASIS, S. 2012 Wavy regimes of film flow down a fiber. *Phys. Rev.* E **85** (4), 046302.

RUYER-QUIL, C., TREVELEYAN, P., GIORGIUTTI-DAUPHINÉ, F., DUPRAT, C. & KALLIADASIS, S. 2008 Modelling film flows down a fibre. *J. Fluid Mech.* **603**, 431–462.

SADEGHPOUR, A., OROUMIYEH, F., ZHU, Y., KO, D.D., JI, H., BERTOZZI, A.L. & JU, Y.S. 2021 Experimental study of a string-based counterflow wet electrostatic precipitator for collection of fine and ultrafine particles. *J. Air Waste Manage. Assoc.* **71** (7), 851–865.

SADEGHPOUR, A., ZENG, Z., JI, H., DEHDARI EBRAHIMI, N., BERTOZZI, A.L. & JU, Y.S. 2019 Water vapor capturing using an array of traveling liquid beads for desalination and water treatment. *Sci. Adv.* **5** (4), eaav7662.

SADEGHPOUR, A., ZENG, Z. & JU, Y.S. 2017 Effects of nozzle geometry on the fluid dynamics of thin liquid films flowing down vertical strings in the Rayleigh–Plateau regime. *Langmuir* **33** (25), 6292–6299.

SHEN, A.Q., GLEASON, B., MCKINLEY, G.H. & STONE, H.A. 2002 Fiber coating with surfactant solutions. *Phys. Fluids* **14** (11), 4055–4068.

SHI, W., ANDERSON, M.J., TULKOFF, J.B., KENNEDY, B.S. & BOREYKO, J.B. 2018 Fog harvesting with harps. *ACS Appl. Mater. Interfaces* **10** (14), 11979–11986.

TRIFONOV, Y.Y. 1992 Steady-state traveling waves on the surface of a viscous liquid film falling down on vertical wires and tubes. *AIChE J.* **38** (6), 821–834.

UCHIYAMA, K., MIGITA, H., OHMURA, R. & MORI, Y.H. 2003 Gas absorption into 'string-of-beads' liquid flow with chemical reaction: application to carbon dioxide separation. *Intl J. Heat Mass Transfer* **46** (3), 457–468.

VAN HULLE, J., DELFORGE, C., LÉONARD, M., FOLLET, E. & VANDEWALLE, N. 2024 Droplet helical motion on twisted fibers. *Langmuir*. **40** (48), 25413–25419.

WAGSTAFF, C., AL-JUAIED, M., PRABHUDHARWADKAR, D. & ROBERTS, W.L. 2024 Wetted-wire columns: a potential alternative to packed or spray columns. *Rev. Chem. Engng* **40** (5), 601–622.

WAGSTAFF, C., GUBBA, S.R., TRUSCOTT, T., ALGASHGARI, K. & ROBERTS, W.L. 2023 Wire density for a wetted-wire column. *Chem. Engng Sci.* **273**, 118633.

WANG, P., ZHOU, J., XU, B., LU, C., MENG, Q. & LIU, H. 2020 Bioinspired anti-Plateau–Rayleigh-instability on dual parallel fibers. *Adv. Mater.* **32** (45), 2003453.

XIE, Q., LIU, R., WANG, X. & CHEN, X. 2021 Investigation of flow dynamics of thin viscous films down differently shaped fibers. *Appl. Phys. Lett.* **119** (20), 201601.

XU, B., SHI, Z., LU, C., HU, Z., CHENG, Y., ZHU, M., JIANG, L. & LIU, H. 2024 Continuous homogeneous thin liquid film on a single cross-shaped profiled fiber with high off-circularity: toward quick-drying fabrics. *Adv. Mater.* **36** (44), 2403316.

YU, L. & HINCH, J. 2014 Drops of power-law fluids falling on a coated vertical fibre. *J. Fluid Mech.* **751**, 184–215.

ZENG, Z., SADEGHPOUR, A. & JU, Y.S. 2018 Thermohydraulic characteristics of a multi-string direct-contact heat exchanger. *Intl J. Heat Mass Transfer* **126**, 536–544.

ZENG, Z., SADEGHPOUR, A. & JU, Y.S. 2019 A highly effective multi-string humidifier with a low gas stream pressure drop for desalination. *Desalination* **449**, 92–100.

ZENG, Z., SADEGHPOUR, A., WARRIER, G. & JU, Y.S. 2017 Experimental study of heat transfer between thin liquid films flowing down a vertical string in the Rayleigh-Plateau instability regime and a counterflowing gas stream. *Intl J. Heat Mass Transfer* **108**, 830–840.

ZHANG, Y., LIU, R. & CHEN, X. 2023 Investigation of the dynamics of a coating flow on a vertical fiber immersed in surrounding liquid phase. *Microgravity Sci. Technol.* **35** (4), 40.